ACS OMEGA

http://pubs.acs.org/journal/acsodf

Article

$CoAl_2O_4$–g-C_3N_4 Nanocomposite Photocatalysts for Powerful Visible-Light-Driven Hydrogen Production

Amal Basaleh* and M. H. H. Mahmoud

Cite This: *ACS Omega* 2021, 6, 10428–10436

Read Online

ACCESS | Metrics & More | Article Recommendations | Supporting Information

ABSTRACT: There is no doubt that the rate of hydrogen production via the water splitting reaction is profoundly affected to a remarkable degree based on the isolation of photogenerated electrons from holes. The precipitation of any cocatalysts on the substrate surfaces (including semiconductor materials) provides significant hindrance to such reincorporation. In this regard, a graphite-like structure in the form of mesoporous g-C_3N_4 formed in the presence of a template of mesoporous silica has been synthesized via the known combustion method. Hence, the resulting g-C_3N_4 nanosheets were decorated with varying amounts of mesoporous $CoAl_2O_4$ nanoparticles (1.0–4.0%). The efficiencies of the photocatalytic H_2 production by $CoAl_2O_4$-doped g-C_3N_4 nanocomposites were studied and compared with those of pure $CoAl_2O_4$ and g-C_3N_4. Visible light irradiation was carried out in the presence of glycerol as a scavenger. The results showed that the noticeable photocatalytic enhancement rate was due to the presence of $CoAl_2O_4$ nanoparticles distributed on the g-C_3N_4 surface. The 3.0% $CoAl_2O_4$–g-C_3N_4 nanocomposite had the optimum concentration. This photocatalyst showed extremely high photocatalytic activities that were up to 22 and 45 times greater than those of $CoAl_2O_4$ and g-C_3N_4, respectively. This photocatalyst also showed 5 times higher photocatalytic stability than that of $CoAl_2O_4$ or g-C_3N_4. The presence of $CoAl_2O_4$ nanoparticles as a cocatalyst increased both the efficiency and productivity of the $CoAl_2O_4$–g-C_3N_4 photocatalyst. This outcome was attributed to the mesostructures being efficient charge separation carriers with narrow band gaps and high surface areas, which were due to the presence of $CoAl_2O_4$.

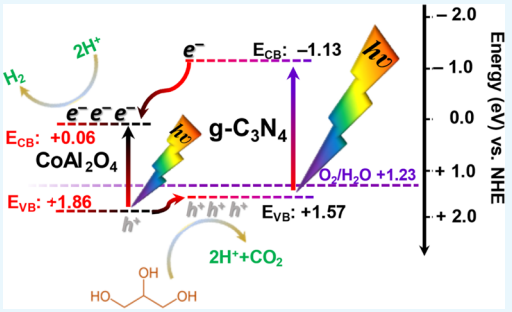

1. INTRODUCTION

Currently, fossil fuels have been used to yield approximately 80% of energy used in the world; hence, an increasing number of environmental problems and crises have been declared. To overcome these problems, many ecofriendly sources of renewable energy have been classified as important for potential evolution and progress. Starting from this point, many researchers have developed the use of another type of fuel, that is, hydrogen produced from water splitting photocatalytic systems. These cells used are functional designs used to obtain clean energy.[1−3] In the past decade, a photoelectrochemical water splitting process for the production of hydrogen and oxygen in the presence of TiO_2 was reported by Fujishima and Honda.[4] This type of conversion involves the transformation of solar energy to another form of energy, chemical energy. This conversion can be carried out using different photocatalysts and constitutes an efficient and appropriate solution to overcome the most obvious energy and environmental problems.

In addition, two-dimensional semiconductor photocatalysts have received considerable attention as a result of the photocatalytic response that they exhibit to visible light.[5,6] Among these materials, graphitic carbon nitride, g-C_3N_4, is a polymeric metal-free semiconductor with a band gap energy (E_g) of approximately 2.7 eV, enabling it to absorb the visible light. It also exhibits many other characteristics, including nontoxicity, excellent stability, low cost, and versatile structural properties.[7,8] The drawbacks of g-C_3N_4 nanosheets have been widely reported in various studies.[7−9] Metal or nonmetal doping, semiconductor coupling, and construction of porous structures are some of the solutions used to avoid these drawbacks.[10−13] However, these proposed structures still suffer from a significant number of disadvantages, including the fast recombination of electron–hole pairs and insufficient absorption of visible light. Pristine g-C_3N_4 still displays a considerably limited performance with respect to photocatalytic activity.[14] Heterostructures containing g-C_3N_4 have been calcified to produce the best g-C_3N_4 compositions in the photocatalysis field, which noticeably promoted photocatalytic achievements among all previously known types. This outcome may result from the development of charge carrier separation, which occurs with each of the catalysts g-C_3N_4/Ag_2MoO_4, g-C_3N_4/Bi_2O_4, g-C_3N_4/perovskite oxide, and g-C_3N_4/TiO_2.[14−19] Combined

Received: February 17, 2021
Accepted: April 1, 2021
Published: April 8, 2021

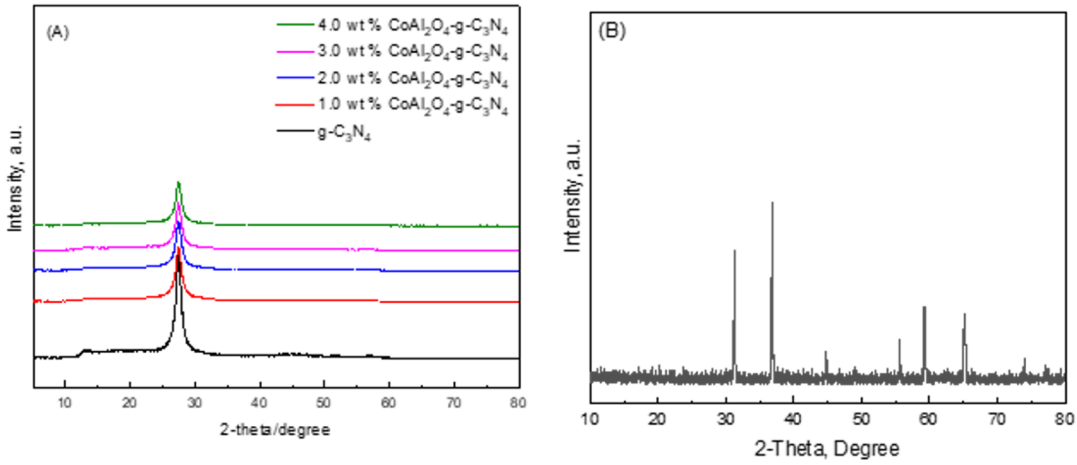

Figure 1. (A): XRD patterns of g-C_3N_4 and $CoAl_2O_4$−g-C_3N_4 samples. (B)XRD diffraction pattern of the prepared pure $CoAl_2O_4$ sample.

semiconductors containing $CoAl_2O_4$ have been utilized for photocatalytic decomposition. $CoAl_2O_4$ also has a narrow band gap of 1.80 eV and exhibits a strong response to visible light.[20−30] To the best of our knowledge, hydrogen production using $CoAl_2O_4$−g-C_3N_4 photocatalysts has not been reported. In this regard, heterostructure-based $CoAl_2O_4$ and mesoporous g-C_3N_4 for the formation of $CoAl_2O_4$−g-C_3N_4 were synthesized by simple sol−gel procedures. The chemical structures of the resulting products were confirmed using various techniques. The photocatalytic activities were evaluated for hydrogen production under visible light. Finally, a likely hydrogen production mechanism for the mesoporous $CoAl_2O_4$−g-C_3N_4 heterostructured nanocomposites was also proposed.

2. EXPERIMENTAL SECTION

2.1. Materials. EO106-PO70EO106 surfactant was used as a triblock copolymer with an average MW of 12,600 g/mol (F-127). $Co(NO_3)_2{\cdot}6H_2O$, $Al(NO_3)_3{\cdot}9H_2O$, acetic acid, hydrochloric acid, and ethanol were all purchased from Sigma-Aldrich.

2.2. Preparation of Mesoporous $CoAl_2O_4$. A sol−gel procedure was used to prepare mesoporous $CoAl_2O_4$ using a structure-directing agent, namely, the F127 triblock copolymer. The required material was synthesized using molar ratios on the order of 1:0.02:50:2.25:3.75 for $CoAl_2O_4$/F127/C_2H_5OH/HCl/CH_3COOH, respectively. For example, a solution of 1.6 g of F127 in 30 mL of ethanol was stirred for 60 min. Next, 0.74 mL of HCl and 2.3 mL of CH_3COOH were added to the previous solution, and magnetic stirring was continued for 30 min. Co and Al precursors were weighed out in a 1:2 ratio and added to the F127−CH_3COOH mesophase with additional stirring for 60 min. A humidity chamber (40%) was used to hold the prepared mesophase at 40 °C for 12 h to reduce the amount of ethanol, leading to the formation of a gel. Further aging at 65 °C for 24 h was carried out in the resulting gel. Finally, the samples were calcined at 600 °C at a heating rate of 1°C/min in air for 4 h and then cooled at a rate of 2°C/min in order to eliminate the F127 surfactant and obtain the mesoporous $CoAl_2O_4$ as a final product.

2.3. Synthesis of Mesoporous g-C_3N_4. Urea and dicyandiamide were purchased from Sigma-Aldrich. High-surface-area mesoporous silica (HMS) (~500−1000 $m^2\ g^{-1}$) was used to prepare g-C_3N_4 with a large surface area. Furthermore, pyrolysis of dicyandiamide and urea in air was performed. The detailed HMS preparation was easily executed as reported in the literature.[31] Approximately 50 mL of distilled water and 1 g of HMS were dispersed for 30 min. A mixture of dicyandiamide (3 g) and urea (5 g) was carefully added to the abovementioned solution. Continuous stirring at 80 °C was done to enhance the dissolution of both components. The sample was dried overnight at approximately 80 °C to remove the excess water. Calcination was performed at 550 °C for 4 h. Next, the obtained material was immersed in a solution of NH_4HF_2 (2 M, 50 mL) with vigorous stirring for 24 h to drive out the HMS template. To release any contaminants adsorbed by the produced g-C_3N_4 nanoparticles, they were easily cleaned by washing several times with water. Thereafter, the synthesized pure material was dried by heating for 12 h at 100 °C.

2.4. Synthesis of Mesoporous $CoAl_2O_4$−g-C_3N_4 Nanocomposites. A water exfoliation method was used to synthesize $CoAl_2O_4$−g-C_3N_4 nanocomposites. The samples were synthesized as follows: 0.2 g of the as-prepared g-C_3N_4 was mixed with the required amount of mesoporous $CoAl_2O_4$, and the mixture was then sonicated in 400 mL of deionized water for 3 h at a power of 40 kHz. This procedure allowed the formation of thin-layered $CoAl_2O_4$−g-C_3N_4 products. A centrifugation process was used to collect the final products with the general abbreviation $x$$CoAl_2O_4$−g-$C_3N_4$, where the nominal molar content of $CoAl_2O_4$ was represented by "x" in this formulation (x = 1, 2, 3, and 4%).

2.5. Characterization. A JEOL JEM-1230 transmission electron microscope was used to determine the images of the prepared samples at 200 kV. Phase identification of the prepared materials was carried out using a Bruker AXS D8 Endeavor X-ray diffractometer. A Nova 2000 series Chromatech apparatus was used to determine the texture properties of the prepared photocatalysts. A Shimadzu system (RF-5301, Japan) was applied for the determination of the photoluminescence (PL) spectra of the prepared photocatalysts. The photocurrent intensity of the prepared photocatalysts was determined using a Zahner Zennium electrochemical workstation. The Fourier transform infrared (FT-IR) spectrum was measured in a KBr dispersion in the range of 400−4000 cm^{-1} using a PerkinElmer spectrometer. A V-570 spectrophotometer (Jasco, Japan) was used to obtain the UV−vis−NIR spectra. The band gap values were determined by UV−vis diffuse reflectance spectroscopy.

2.6. Photocatalytic Tests. A certain quantity of the photocatalyst was suspended in 450 mL of H_2O in the presence of a glycerol scavenger (10% vol) prior to the production of

https://doi.org/10.1021/acsomega.1c00872
ACS Omega 2021, 6, 10428−10436

hydrogen. The required experiments were carried out under normal conditions at room temperature and atmospheric pressure. To overcome the effect of lamp heating on the reaction, a cooler made from quartz was used. Before photocatalysis began, nitrogen gas was bubbled for 30 min to eliminate oxygen dissolved in water. The area above the photoreactor was fixed with a 500 W xenon lamp producing visible light. The photocatalytic process for H_2 production started when the lamp was switched on. An Agilent GC 7890A gas chromatograph with nitrogen carrier gas was used to examine the quantity of H_2 produced over separate periods of time throughout the photocatalytic process. Further reactions, as additional confirmations of the optimized parameters, were carried out without a lighting source and without the desired photocatalyst.

3. RESULTS AND DISCUSSION

3.1. Investigation of the Product Samples. The X-ray diffraction (XRD) patterns for the pure g-C_3N_4 and $CoAl_2O_4$−g-C_3N_4 nanocomposites are illustrated in Figure 1A. The XRD diffraction patterns for pure $CoAl_2O_4$ are illustrated in Figure 1A,B. All the diffraction patterns obtained confirm the suggested structures. g-C_3N_4 was indicated by the diffraction peak observed at 27.4° in Figure 1A, according to card number JCPDS 87-1526. On the other hand, the XRD diffractogram assigned to pure $CoAl_2O_4$ corresponded to that in card number JCPDS 044-0160, as all essential peaks have been mentioned. These peaks are attributed to the $CoAl_2O_4$ phase, as shown in Figure 1B. The diffractograms also show that the g-C_3N_4 peak intensities showed considerable decreases as the $CoAl_2O_4$ content increased (1.0−4.0%). All $CoAl_2O_4$−g-C_3N_4 diffractograms show that no additional peaks related to pure $CoAl_2O_4$ were still present, which is attributed to the strong $CoAl_2O_4$ adhesion to the surface of g-C_3N_4 nanosheets. Additionally, this result was attributed to the lower $CoAl_2O_4$ content present in each composition. The XRD diffraction patterns also showed no additional equivocal peaks in any samples. This observation provides good evidence for the formation of the heterojunction nanocomposite between $CoAl_2O_4$ and g-C_3N_4 nanosheets.

The FT-IR spectra of the prepared pure $CoAl_2O_4$, g-C_3N_4, and $CoAl_2O_4$−g-C_3N_4 samples are illustrated in Figure 2. The triazine stretching mode present in both the pure g-C_3N_4 and $CoAl_2O_4$−g-C_3N_4 nanocomposites was observed at 808 cm^{-1}. Along with the peaks for the typical CN-heterocyclic stretching modes, five additional peaks were observed at 1633, 158, 1408, 1322, and 1243 cm^{-1}.[32−34] The FT-IR spectra also revealed that the intensity of the peak for pure g-C_3N_4 was significantly reduced as the $CoAl_2O_4$ content increased. An absorption peak at approximately 664 cm^{-1} was also present in the FT-IR spectrum of pure $CoAl_2O_4$ nanoparticles.

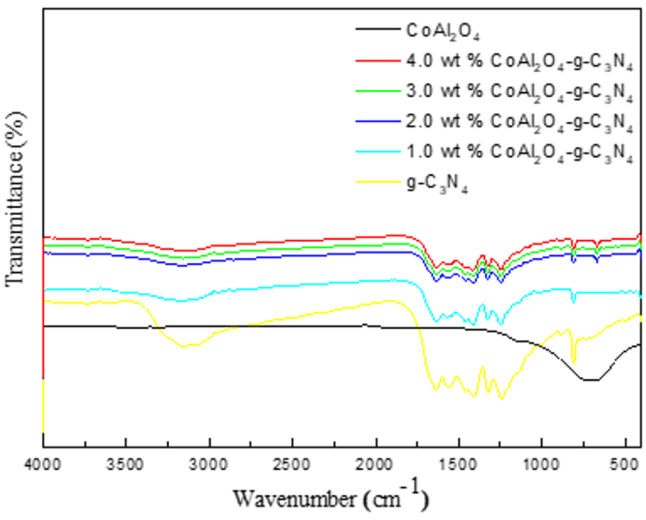

Figure 2. FT-IR spectra of pure $CoAl_2O_4$, g-C_3N_4, and $CoAl_2O_4$−g-C_3N_4 samples.

The X-ray photoelectron spectroscopy analysis for the 3.0% $CoAl_2O_4$−g-C_3N_4 nanocomposite is shown in Figure 3. The high-resolution spectra of Co, Al, O, C, and N are shown in Figure 3A−E. The presence of Co^{2+} and Co^{3+} ions in the prepared nanocomposites was confirmed by the presence of the major peaks assigned to Co $2p_{1/2}$ at ∼794.7 and 804.2 eV and Co $2p_{3/2}$ at ∼779 eV and 783.6 eV (Figure 3A). It is easily determined that the obtained values are very similar to those reported in the literature.[35] Furthermore, Figure 3B displays one peak for Al 2p at 73.5 eV, confirming the presence of Al as Al oxide.[36] Furthermore, Figure 3C shows that the O 1s spectrum consists of two peaks at 531 and 530 eV that could be related to the adsorbed oxygen species and $CoAl_2O_4$ lattice oxygen, respectively.[37,38] Two main C 1s peaks at ∼287.9 and ∼284.6 eV were also detected, as shown in Figure 3D. These peaks indicate the presence of sp^2 C connected to N in the N-containing aromatic rings and sp^2 C−C bonds. Figure 3E shows that the N 1s peak appears at 398.3 eV, which reveals the presence of sp^2-hybridized N atoms. The structure of graphitic carbon nitride g-C_3N_4 was confirmed by all the abovementioned information.[39]

The transmission electron microscopy (TEM) images of the $CoAl_2O_4$, g-C_3N_4, and 3.0% $CoAl_2O_4$−g-C_3N_4 samples are displayed in Figure 4. The average particle sizes of the prepared $CoAl_2O_4$ nanoparticles were in the 5−8 nm range (Figure 4A). The typical nanosheet structure of g-C_3N_4 is shown in Figure 4B. The TEM images of the $CoAl_2O_4$−g-C_3N_4 nanocomposite are shown in Figure 4C and exhibit a considerable dispersion of $CoAl_2O_4$, in the form of spherical particles, over the g-C_3N_4 nanosheet. In addition, a significant decoration of $CoAl_2O_4$ has been noted. Figure 4D shows the high-resolution transmission electron microscopy (HRTEM) image of the 3.0% $CoAl_2O_4$−g-C_3N_4 nanocomposite product. Examination of the image confirms the higher distribution of $CoAl_2O_4$ on the g-C_3N_4 surface. The existence of g-C_3N_4 and $CoAl_2O_4$ was also confirmed by the determination of lattice spacings of 0.320 and 0.460 nm for the (002) and (111) planes, respectively.[39] Hence, a strong interfacial interaction between g-C_3N_4 and $CoAl_2O_4$ is clearly revealed by the HRTEM image.

The surface properties of the obtained nanocomposites were explored, and Figure 5 demonstrates the N_2 adsorption−desorption isotherms for the g-C_3N_4, $CoAl_2O_4$, and 3.0% $CoAl_2O_4$−g-C_3N_4 samples. As per the IUPAC convention, the obtained isotherms are classified as IV-type isotherms, which are indicative of mesostructured materials. This observation indicates that after the dispersion of $CoAl_2O_4$ nanoparticles over the g-C_3N_4 nanosheets, the mesoporous characteristics remain without any changes. The surface areas of g-C_3N_4, pure $CoAl_2O_4$, and various loadings of $CoAl_2O_4$ on g-C_3N_4 are listed in Table 1. As the results show, the surface area of pure g-C_3N_4 is 175 m^2/g, which is considerably larger than the reported literature value.[40] This increase in the obtained surface area is mainly the result of the presence of the initial HMS precursor, as previously highlighted in the Experimental Section. The slight decrease due to the presence of $CoAl_2O_4$ could be attributed to

https://doi.org/10.1021/acsomega.1c00872
ACS Omega 2021, 6, 10428−10436

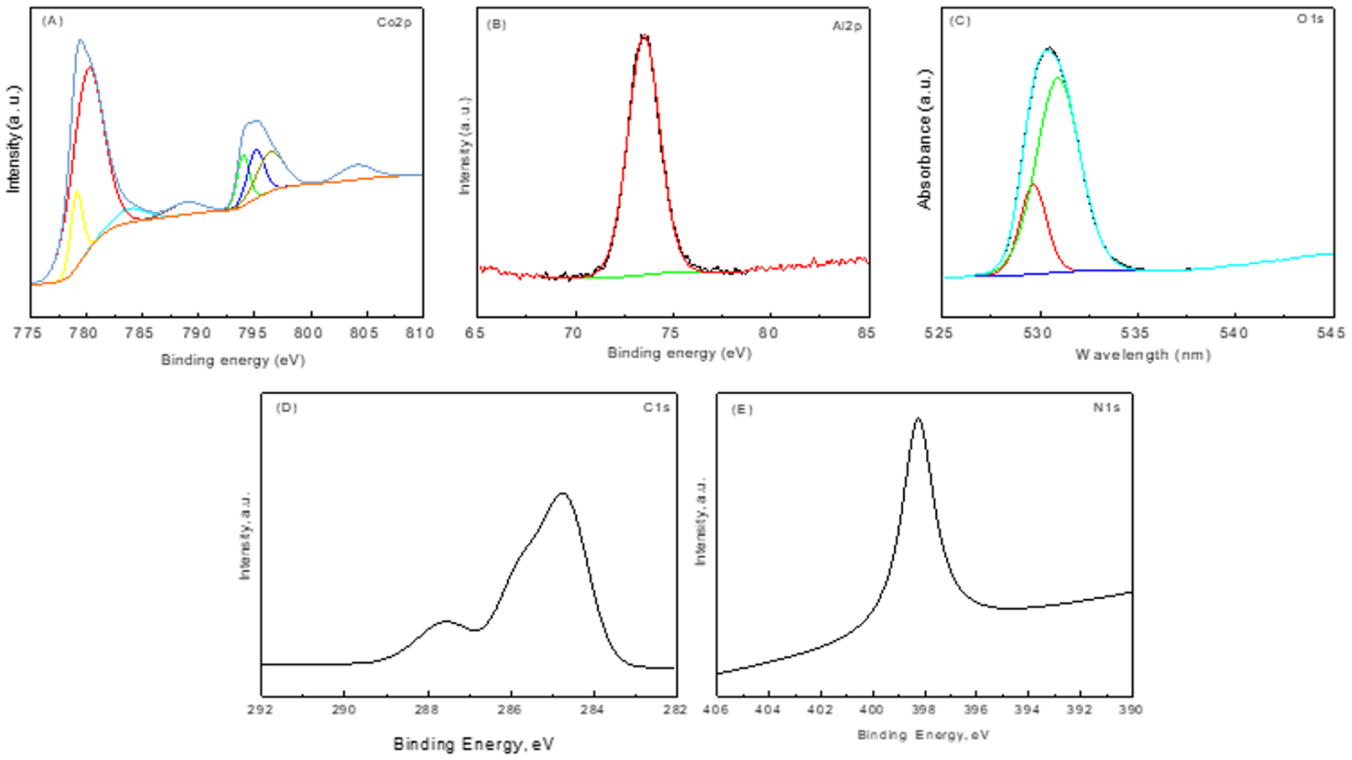

Figure 3. High-resolution spectra of 3.0 wt % $CoAl_2O_4$–g-C_3N_4 for Co 2p (A), Al 2p (B), O 1s (C), C 1s (D), and N 1s (E) species.

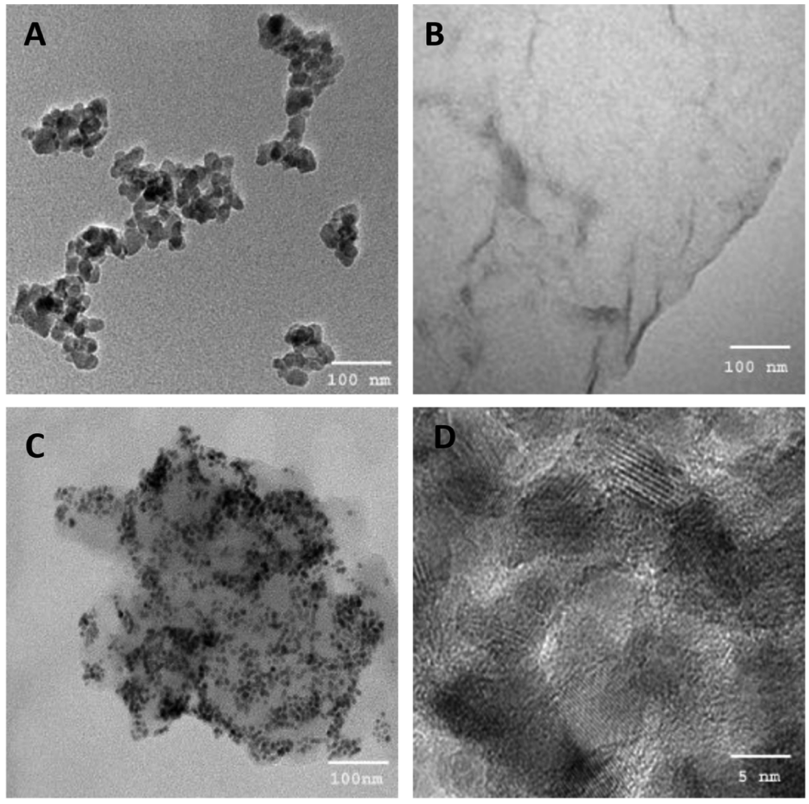

Figure 4. TEM images of $CoAl_2O_4$ (A), g-C_3N_4 (B), and 3.0 wt % $CoAl_2O_4$–g-C_3N_4 (C) samples, and (D) HRTEM image of the 3.0 wt % $CoAl_2O_4$–g-C_3N_4 sample.

the pore filling of C_3N_4 with homogeneously dispersed particles on the surface.

Figure 6 illustrates the UV–vis spectra of the pure $CoAl_2O_4$, g-C_3N_4, and $CoAl_2O_4$–g-C_3N_4 photocatalysts with varying $CoAl_2O_4$ contents. The results confirm the absorption of visible light by all samples. The presence of $CoAl_2O_4$ also enhanced the width of both the absorption bands and band edges (Figure 6). UV–vis spectra were also used to determine the band gaps in all

https://doi.org/10.1021/acsomega.1c00872
ACS Omega 2021, 6, 10428–10436

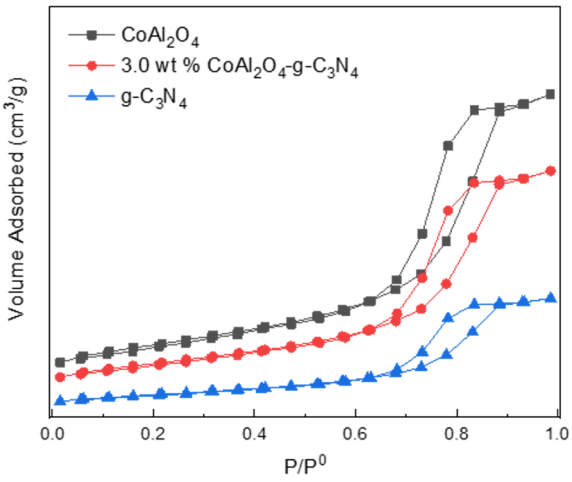

Figure 5. N_2 adsorption−desorption isotherms for the g-C_3N_4, $CoAl_2O_4$, and 3.0% $CoAl_2O_4$−g-C_3N_4 samples.

Table 1. BET Surface Areas of g-C_3N_4 and $CoAl_2O_4$@g-C_3N_4 Samples

samples	SBET (m^2/g)
g-C_3N4	175.00
1.0 wt % $CoAl_2O_4$@g-C_3N4	184.00
2.0 wt % $CoAl_2O_4$@g-C_3N4	188.00
3.0 wt % $CoAl_2O_4$@g-C_3N4	192.00
4.0 wt % $CoAl_2O_4$@g-C_3N4	193.00
$CoAl_2O_4$	210.00

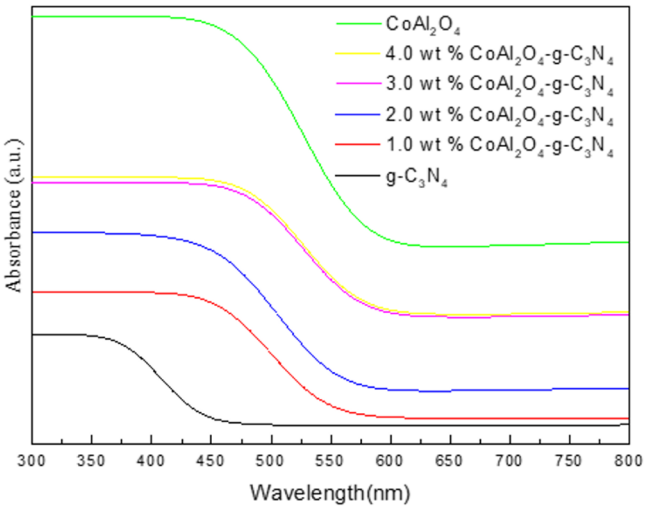

Figure 6. UV−vis spectra of pure $CoAl_2O_4$, g-C_3N_4, and $CoAl_2O_4$−g-C_3N_4 samples with various $CoAl_2O_4$ contents.

cases, and the outcomes are listed in Table 2. The calculated values of the band gaps of g-C_3N_4 were heavily affected by the loading percentage of $CoAl_2O_4$ in the nanocomposites. Consistently, the band gap was reduced as the integrated weight percentage of $CoAl_2O_4$ on the surface of the g-C_3N_4 nanosheets was increased.

3.2. Evolution of H_2 via Visible Light Irradiation with the Obtained Catalysts. The targeted $CoAl_2O_4$−g-C_3N_4 nanocomposite photocatalysts were examined and compared with pure $CoAl_2O_4$ and g-C_3N_4 for hydrogen production upon irradiation with visible light. The initial reaction conditions included a photocatalyst content of 1.2 g/L, a reaction solution

Table 2. Band Gaps of g-C_3N_4 and $CoAl_2O_4$@g-C_3N_4 Samples

samples	band gap, eV
g-C_3N_4	2.70
1.0 wt % $CoAl_2O_4$@g-C_3N_4	2.20
2.0 wt % $CoAl_2O_4$@g-C_3N_4	2.10
3.0 wt % $CoAl_2O_4$@g-C_3N_4	1.94
4.0 wt % $CoAl_2O_4$@g-C_3N_4	1.92
$CoAl_2O_4$	1.80

volume of 450 mL, the presence of glycerol (10 vol %), a Xe lamp (500 W) light source, and 9 h of irradiation at room temperature. The effect of different $CoAl_2O_4$ loadings from 1.0 to 4.0 wt % in the $CoAl_2O_4$−g-C_3N_4 nanocomposite on the quantity of hydrogen produced was studied and compared with the volumes obtained with both pure $CoAl_2O_4$ and g-C_3N_4, as illustrated in Figure 7A. The results revealed that the quantities of hydrogen produced were 810 and 400 μmol g^{-1} for $CoAl_2O_4$ nanoparticles and g-C_3N_4 nanosheets, respectively. The use of various weight percentages in the $CoAl_2O_4$−g-C_3N_4 samples (1.0, 2.0, 3.0, and 4.0 wt %) used for the generation of hydrogen resulted in 1912, 9450, 13050, and 13,095 μmol g^{-1} of hydrogen, respectively. The values are greater than those in some published works[40,41] and less than those in other published works.[42−44] Thus, the results obtained indicated that the addition of $CoAl_2O_4$ nanoparticles significantly increased the extent of charge carrier separation and the surface area and decreased the band gap energy. Therefore, the $CoAl_2O_4$ content in the original photocatalyst showed a direct and positive effect on the H_2 yield until a certain loading weight (3.0%) was reached. Above this weight percentage, there was no additional effect on the yield, which did not respond to the addition of any extra photocatalyst in the reaction mixture. The production of hydrogen was increased to 8775, 10,125, 13,050, 16,875, and 18,225 μmol g^{-1} as a result of the gradual increase in the content of photocatalyst from 0.4 to 2.0 g/L, as shown in Figure 7B. These results may have occurred because the total number of active sites over the 3.0% $CoAl_2O_4$−g-C_3N_4 photocatalyst surface showed a noticeable increase. The level of hydrogen production was at least 15,120 μmol g^{-1} when the photocatalyst content was greater than 2.4 g/L. This result may be due to an effective reduction in light penetration during the illumination process in the presence of a higher particle content in the reaction solution.[45−49]

The measurements of both PL and transient photocurrent responses emphasize the results obtained in this study. As seen in Figure 8A, the PL spectrum of g-C_3N_4 shows the highest PL emission intensity among all samples. However, upon increasing the content of $CoAl_2O_4$ nanoparticles adsorbed over the g-C_3N_4 nanosheet surface, the PL emission intensity noticeably decreased, as illustrated. The observed PL emission intensities decreased as follows: g-C_3N_4 > $CoAl_2O_4$ > 1.0% $CoAl_2O_4$−g-C_3N_4 > 2.0% $CoAl_2O_4$−g-C_3N_4 > 3.0% $CoAl_2O_4$−g-C_3N_4 ≈ 4.0% $CoAl_2O_4$−g-C_3N_4. The $CoAl_2O_4$ nanoparticles have a high PL emission intensity and show a lower band gap energy (1.80 eV). Therefore, $CoAl_2O_4$ displays a low photocatalytic activity, and the recombination rate of the charge carriers in the presence of $CoAl_2O_4$ is very high. However, the photocatalyst effectiveness remains clear and apparent from the standpoint of photocatalytic activity. The photocurrent transient responses are given in Figure 8B. The results indicate that a lower photocurrent density was observed for g-C_3N_4, while a substantial increase occurred as the content of $CoAl_2O_4$

https://doi.org/10.1021/acsomega.1c00872
ACS Omega 2021, 6, 10428−10436

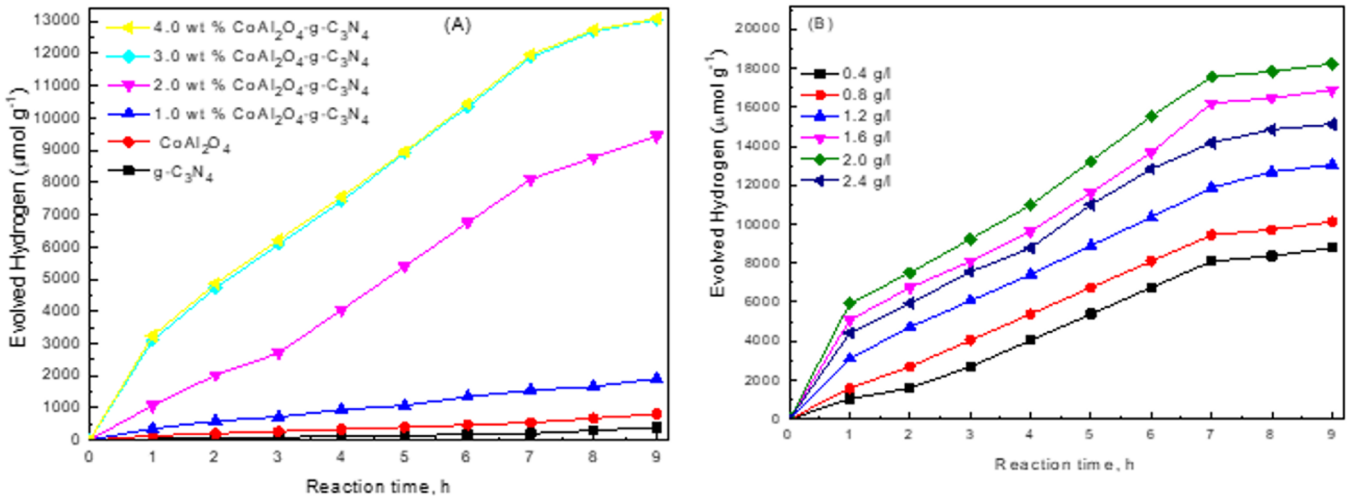

Figure 7. (A) Effect of $CoAl_2O_4$ content on hydrogen evolved using the g-C_3N_4 photocatalyst. (B) Effect of the amount of 3.0% $CoAl_2O_4$–g-C_3N_4 photocatalyst used for hydrogen evolution.

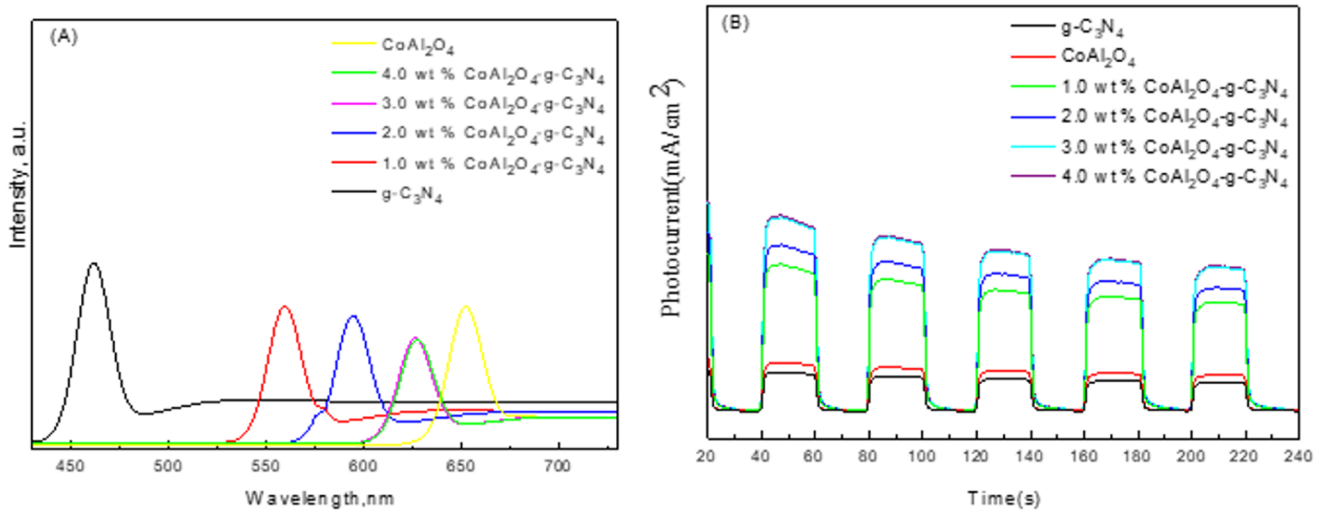

Figure 8. (A) PL spectra of pure $CoAl_2O_4$, g-C_3N_4, and $CoAl_2O_4$–g-C_3N_4 samples with various $CoAl_2O_4$ contents. (B) Photocurrent transient responses of pure $CoAl_2O_4$, g-C_3N_4, and $CoAl_2O_4$–g-C_3N_4 samples with various $CoAl_2O_4$ contents.

deposited on the surface of g-C_3N_4 increased. The photocurrent densities of the designed nanocomposites increased in the following order: g-C_3N_4 < $CoAl_2O_4$ < 1.0% $CoAl_2O_4$–g-C_3N_4 < 2.0% $CoAl_2O_4$–g-C_3N_4 < 3.0% $CoAl_2O_4$–g-C_3N_4 ≈ 3.0% $CoAl_2O_4$–g-C_3N_4. These outcomes also show that the success of the photocatalytic process for the $CoAl_2O_4$–g-C_3N_4 nanocomposites coincides closely with, and is proportional to, the results of the PL measurements.

Figure 9 shows the photocatalytic reproducibility of reused photocatalysts. As previously mentioned, the 3.0% $CoAl_2O_4$–g-C_3N_4 photocatalyst contains the optimum composition and shows substantial recycling potential. $CoAl_2O_4$–g-C_3N_4 may be recycled five times without exhibiting any significant defects. The fifth round affords 99.7% of the hydrogen evolution efficiency observed in the first use. From the above results, the optimized photocatalyst, 3.0% $CoAl_2O_4$–g-C_3N_4, demonstrated high stability, representing a highly applicable and valuable photocatalyst for the evolution of hydrogen. The XRD, UV–vis, and PL characterizations of the photocatalysts used also confirmed that the photocatalysts are stable. Additionally, inductively coupled plasma analysis of the solution remaining after catalysis confirmed that there were no Co or Al ions present, which confirmed the stability of the photocatalyst.

3.3. Suggested Mechanism for the $CoAl_2O_4$–g-C_3N_4 Nanocomposite. The separation of photoelectrons and holes in g-C_3N_4 nanosheet-reinforced $CoAl_2O_4$ nanoparticles has been explained by using the proposed mechanism below (Scheme 1). The following equations have been used to calculate the band energy levels

$$E_{CB} = X - 0.5E_g + E_0 \quad (1)$$

$$E_{VB} = E_g + E_{CB} \quad (2)$$

where the valence and conduction bands are designated E_{VB} and E_{CB}, respectively; the band gap value is given as E_g and is determined from optical measurements; the absolute electronegativity of the semiconductor is represented as X; and the normal hydrogen electrode versus the redox-level measurement on the absolute vacuum scale is given as E_0 (E_0 = −4.5 eV). A narrow band gap value for g-C_3N_4 nanosheets has been previously reported. Hence, a lower energy is required to excite the system. As a result of the photocatalytic irradiation, the

https://doi.org/10.1021/acsomega.1c00872
ACS Omega 2021, 6, 10428−10436

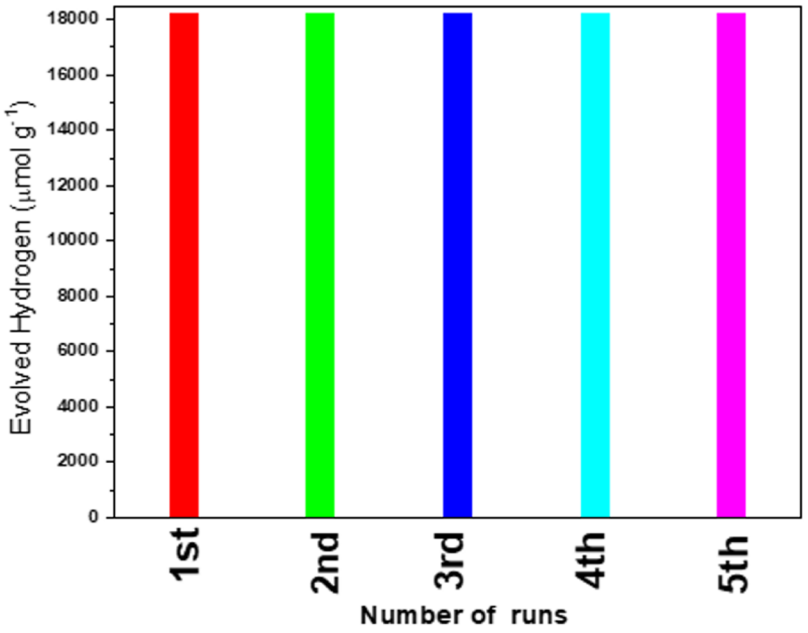

Figure 9. Reuse and reproducibility of 3.0 wt % $CoAl_2O_4$–g-C_3N_4 photocatalyst used five times.

Scheme 1. Photocatalytic Process of the 3.0 wt % $CoAl_2O_4$–g-C_3N_4 Photocatalyst for Hydrogen Production

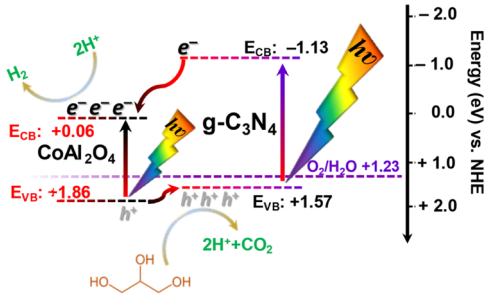

photogenerated electrons from pure g-C_3N_4 originate from the valance band and are promoted to the conduction band. However, in the $CoAl_2O_4$–g-C_3N_4 nanocomposite, $CoAl_2O_4$ accepts the excited electrons, thereby realizing the desired charge carrier separation. The energy of the $CoAl_2O_4$ conduction band (+0.06 eV) exhibits a more positive value than that of g-C_3N_4 (−1.13 eV). Additionally, the distribution of $CoAl_2O_4$ nanoparticles across the g-C_3N_4 nanosheets in the nanocomposites provides a noticeable increase in the number of active sites on the $CoAl_2O_4$–g-C_3N_4 photocatalyst surface; the photocatalytic activity is enhanced and hydrogen production is considerably accelerated relative to either $CoAl_2O_4$ or g-C_3N_4. In total, the gross efficiency of the hole-scavenging action is greatly increased because the reaction solution contains glycerol as a scavenger. Protons are readily produced by this process and can additionally react with charge carriers to create more H_2. Therefore, according to Scheme 1, water splitting can occur at 1.23 eV according to ref 50, which lies within the band gap of g-C_3N_4. CO_2 formation is an obvious product of hole transfer from p-type $CoAl_2O_4$ to the attached g-C_3N_4, exhibiting an energy of +1.57 eV. These holes could produce protons and CO_2 from the obvious decomposition of glycerol, as seen in previous literature reports.[51] With the assistance of the separated electrons in the CB of supported $CoAl_2O_4$, hydrogen generation is made possible by the combination of two protons with electrons.

4. CONCLUSIONS

It is easy to prepare g-C_3N_4 nanosheets via a combustion process using a template material of mesoporous silica. Various $CoAl_2O_4$ nanoparticle contents (1.0–4.0%) were used as adsorbents on the g-C_3N_4 nanosheets as a result of the preparation process. The g-C_3N_4 sheets were affected by the dispersion of $CoAl_2O_4$ on the surface of the nanocomposites. Prevention of electron–hole reincorporation was significantly enhanced by the decrease in the band gap energy. The photocatalyst $CoAl_2O_4$–g-C_3N_4 (3.0 wt %) produced 18,225 μmol g^{-1} of hydrogen, the maximum amount produced by the catalysts prepared with various compositions. In addition, a maximum photocatalyst weight of up to 2.0 g/L was used, with irradiation carried out for 9 h at room temperature. The synergetic effect of $CoAl_2O_4$ and g-C_3N_4 enhances the production of hydrogen. The $CoAl_2O_4$–g-C_3N_4 composites produce a significantly greater amount of hydrogen than either the g-C_3N_4 sheets or pure $CoAl_2O_4$ nanoparticles. A highly efficient, stable product has been developed in the form of $CoAl_2O_4$–g-C_3N_4. A maximum of five repeated cycles was also studied, without any loss of hydrogen evolution in any of the cycles.

■ ASSOCIATED CONTENT

Supporting Information

The Supporting Information is available free of charge at https://pubs.acs.org/doi/10.1021/acsomega.1c00872.

Comparison between the quantum efficiencies of different photocatalysts and our prepared photocatalyst (PDF)

■ AUTHOR INFORMATION

Corresponding Author

Amal Basaleh − *Department of Chemistry, Faculty of Science, King Abdulaziz University, Jeddah 21589, Kingdom of Saudi Arabia;* orcid.org/0000-0002-7739-1113;
Email: amalbasaleh1@gmail.com

https://doi.org/10.1021/acsomega.1c00872
ACS Omega 2021, 6, 10428−10436

Author

M. H. H. Mahmoud − *Department of Chemistry, College of Science, Taif University, Taif 21944, Saudi Arabia*

Complete contact information is available at: https://pubs.acs.org/10.1021/acsomega.1c00872

Notes

The authors declare no competing financial interest.

■ ACKNOWLEDGMENTS

The authors would like to thank Taif University Researchers Supporting Project (number TURSP-2020/158) of Taif University, Taif, Saudi Arabia, for supporting this work.

■ REFERENCES

(1) Gray, H. B. Powering the planet with solar fuel. *Nat. Chem.* **2009**, *1*, 7.

(2) Tong, H.; Ouyang, S.; Bi, Y.; Umezawa, N.; Oshikiri, M.; Ye, J. Nano-photocatalytic materials: possibilities and challenges. *Adv. Mater.* **2012**, *24*, 229−251.

(3) Tran, P. D.; Wong, L. H.; Barber, J.; Loo, J. S. C. Recent advances in hybrid photocatalysts for solar fuel production. *Energy Environ. Sci.* **2012**, *5*, 5902−5918.

(4) Fujishima, A.; Honda, K. Electrochemical photolysis of water at a semiconductor electrode. *nature* **1972**, *238*, 37−38.

(5) Mkhalid, I. A.; Shawky, A. Visible light-active CdSe/rGO heterojunction photocatalyst for improved oxidative desulfurization of thiophene. *Ceram. Int.* **2020**, *46*, 20769−20776.

(6) Alhaddad, M.; Shawky, A. Superior photooxidative desulfurization of thiophene by reduced graphene oxide-supported MoS_2 nanoflakes under visible light. *Fuel Process. Technol.* **2020**, *205*, 106453.

(7) W.-J., Ong; L.-L., Tan; Y. H., Ng; S.-T., Yong; S.-P., Chai, Graphitic carbon nitride (g-C_3N_4)-based photocatalysts for artificial photosynthesis and environmental remediation: are we a step closer to achieving sustainability? Chem. Rev. 116 (**2016**, *116*) 7159−7329. DOI: 10.1021/acs.chemrev.6b00075

(8) Nikokavoura, A.; Trapalis, C. Graphene and g-C3N4 based photocatalysts for NOx removal: a review. *Appl. Surf. Sci.* **2018**, *430*, 18−52.

(9) Xu, J.; Wu, H.-T.; Wang, X.; Xue, B.; Li, Y.-X.; Cao, Y. A new and environmentally benign precursor for the synthesis of mesoporous g-C_3N_4 with tunable surface area. *Phys. Chem. Chem. Phys.* **2013**, *15*, 4510−4517.

(10) Tonda, S.; Kumar, S.; Kandula, S.; Shanker, V. Fe-doped and -mediated graphitic carbon nitride nanosheets for enhanced photocatalytic performance under natural sunlight. *J. Mater. Chem. A* **2014**, *2*, 6772−6780.

(11) Cui, Y.; Wang, H.; Yang, C.; Li, M.; Zhao, Y.; Chen, F. Post-activation of in situ BF codoped g-C_3N_4 for enhanced photocatalytic H2 evolution, Appl. *Surf. Sci.* **2018**, *441*, 621−630.

(12) Fu, J.; Jiaguo, Y.; Chuanjia, J.; Bei, C. g-C3N4-based heterostructured photocatalysts. *Adv. Energy Mater.* **2018**, *8*, 1701503.

(13) Ding, F.; Yang, D.; Tong, Z.; Nan, Y.; Wang, Y.; Zou, X.; Jiang, Z. Graphitic carbon nitride-based nanocomposites as visible-light driven photocatalysts for environmental purification. *Environ. Sci.: Nano* **2017**, *4*, 1455−1469.

(14) Li, G.; Nie, X.; Chen, J.; Jiang, Q.; An, T.; Wong, P. K.; Zhang, H.; Zhao, H.; Yamashita, H. Enhanced visible-light-driven photocatalytic inactivation of Escherichia coli using g-C3N4/TiO2 hybrid photocatalyst synthesized using a hydrothermal-calcination approach. *Water Res.* **2015**, *86*, 17−24.

(15) Gao, H.; Jia, J.; Guo, F.; Li, B.; Dai, D.; Deng, X.; Liu, X.; Si, C.; Liu, G. The electronic structure and photoactivity of TiO2 modified by hybridization with monolayer g-C3N4. *J. Photochem. Photobiol., A* **2018**, *364*, 328−335.

(16) Xia, D.; Wang, W.; Yin, R.; Jiang, Z.; An, T.; Li, G.; Zhao, H.; Wong, P. K. Enhanced photocatalytic inactivation of Escherichia coli by a novel Z-scheme g-C3N4/m-Bi2O4 hybrid photocatalyst under visible light: the role of reactive oxygen species. *Appl. Catal., B* **2017**, *214*, 23−33.

(17) Pandiri, M.; Velchuri, R.; Gundeboina, R.; Muga, V. A facile in-situ hydrothermal route to construct a well-aligned β-Ag2MoO4/g-C3N4 heterojunction with enhanced visible light photodegradation: mechanistic views. *J. Photochem. Photobiol., A* **2018**, *360*, 231−241.

(18) Jiang, D.; Wang, T.; Xu, Q.; Li, D.; Meng, S.; Chen, M. Perovskite oxide ultrathin nanosheets/g-C3N4 2D-2D heterojunction photocatalysts with significantly enhanced photocatalytic activity towards the photodegradation of tetracycline. *Appl. Catal., B* **2017**, *201*, 617−628.

(19) Jiang, D.; Ma, W.; Yao, Y.; Xiao, P.; Wen, B.; Li, D.; Chen, M. Dion−Jacobson-type perovskite KCa2Ta3O10 nanosheets hybridized with g-C3N4 nanosheets for photocatalytic H2 production. *Catal. Sci. Technol.* **2018**, *8*, 3767−3773.

(20) Salavati-Niasari, M.; Farhadi-Khouzani, M.; Davar, F. Bright blue pigment $CoAl_2O_4$ nanocrystals prepared by modified sol−gel method. *J. Solgel Sci. Technol.* **2009**, *52*, 321−327.

(21) Mindru, I.; Marinescu, G.; Gingasu, D.; Patron, L.; Ghica, C.; Giurginca, M. Blue CoAl2O4 spinel via complexation method. *Mater. Chem. Phys.* **2010**, *122*, 491−497.

(22) Chang, Y.; Feng, T.; Wu, C.; Chen, Y.; Ke, K.; Liu, Y.; Wang, H.; Dong, S. Controlled synthesis of blue spherical CoAl2O4 pigment powder in Pickering emulsion assisted with a hydrothermal process. *Adv. Powder Technol.* **2018**, *29*, 1222−1229.

(23) Torkian, L.; Daghighi, M. Effects of β-alanine on morphology and optical properties of CoAl2O4 nanopowders as a blue pigment. *Adv. Powder Technol.* **2014**, *25*, 739−744.

(24) Kim, J.-H.; Son, B.-R.; Yoon, D.-H.; Hwang, K.-T.; Noh, H.-G.; Cho, W.-S.; Kim, U.-S. Characterization of blue CoAl2O4 nano-pigment synthesized by ultrasonic hydrothermal method. *Ceram. Int.* **2012**, *38*, 5707−5712.

(25) Gao, H.; Yang, H.; Wang, S.; Li, D.; Wang, F.; Fang, L.; Lei, L.; Xiao, Y.; Yang, G. A new route for the preparation of CoAl2O4 nano blue pigments with high uniformity and its optical properties. *J. Solgel Sci. Technol.* **2018**, *86*, 206−216.

(26) Aly, K. A.; Khalil, N. M.; Algamal, Y.; Saleem, Q. M. A. Lattice strain estimation for CoAl2O4 nano particles using Williamson-Hall analysis. *J. Alloys Compd.* **2016**, *676*, 606−612.

(27) Yu, F.; Yang, J.; Ma, J.; Du, J.; Zhou, Y. Preparation of nanosized CoAl2O4 powders by sol−gel and sol−gel-hydrothermal methods. *J. Alloys Compd.* **2009**, *468*, 443−446.

(28) Chen, J.; Shen, S.; Guo, P.; Wang, M.; Wu, P.; Wang, X.; Guo, L. In-situ reduction synthesis of nano-sized Cu2O particles modifying g-C3N4 for enhanced photocatalytic hydrogen production. *Appl. Catal., B* **2014**, *152*−*153*, 335−341.

(29) Peng, B.; Zhang, S.; Yang, S.; Wang, H.; Yu, H.; Zhang, S.; Peng, F. Synthesis and characterization of g-C3N4/Cu2O composite catalyst with enhanced photocatalytic activity under visible light irradiation. *Mater. Res. Bull.* **2014**, *56*, 19−24.

(30) Ma, X.; Zhang, J.; Wang, B.; Li, Q.; Chu, S. Hierarchical Cu2O foam/g-C3N4 photocathode for photoelectrochemical hydrogen production. *Appl. Surf. Sci.* **2018**, *427*, 907−916.

(31) Mohamed, R. M.; Aazam, E. S. Characterization and Catalytic Properties of Nano-Sized Au Metal Catalyst on Titanium Containing High Mesoporous Silica (Ti-HMS) Synthesized by Photo-Assisted Deposition and Impregnation Methods. *Int. J. Photoenergy* **2011**, *501*, 301.

(32) Liu, W.; Shen, J.; Yang, X.; Liu, Q.; Tang, H. Dual Z-scheme g-C3N4/Ag3PO4/Ag2MoO4 ternary composite photocatalyst for solar oxygen evolution from water splitting. *Appl. Surf. Sci.* **2018**, *456*, 369−378.

(33) Ma, W.; Li, D.; Wen, B.; Ma, X.; Jiang, D.; Chen, M. Construction of novel Sr0.4H1.2Nb2O6·H2O/g-C3N4 heterojunction with enhanced visible light photocatalytic activity for hydrogen evolution. *J. Colloid Interface Sci.* **2018**, *526*, 451−458.

(34) Pu, Y.-C.; Chou, H.-Y.; Kuo, W.-S.; Wei, K.-H.; Hsu, Y.-J. Interfacial charge carrier dynamics of cuprous oxide-reduced graphene

oxide (Cu_2O-rGO) nanoheterostructures and their related visible-light-driven photocatalysis. *Appl. Catal., B* **2017**, *204*, 21−32.
(35) Duan, X.; Pan, M.; Yu, F.; Yuan, D. Synthesis, structure and optical properties of $CoAl_2O_4$ spinel nanocrystals. *J. Alloys Compd.* **2011**, *509*, 1079−1083.
(36) Han, J.-k.; Jia, L.-t.; Hou, B.; Li, D.-b.; Liu, Y.; Liu, Y.-c. Catalytic properties of CoAl2O4/Al2O3 supported cobalt catalysts for fischer-tropsch synthesis. *J. Fuel Chem. Technol.* **2015**, *43*, 846−851.
(37) Wang, J.-C.; Yao, H.-C.; Fan, Z.-Y.; Zhang, L.; Wang, J.-S.; Zang, S.-Q.; Li, Z.-J. Indirect Z-Scheme BiOI/g-C3N4 Photocatalysts with Enhanced Photoreduction CO2 Activity under Visible Light Irradiation. *ACS Appl. Mater. Interfaces* **2016**, *8*, 3765−3775.
(38) Chen, F.; Zhang, X. H.; Hu, X. D.; Zhang, W.; Zeng, R.; Liu, P. D.; Zhang, H. Q. Synthesis and characteristics of nanorods of gadolinium hydroxide and gadolinium oxide. *J. Alloys Compd.* **2016**, *664*, 311−316.
(39) Li, W.; Li, J.; Guo, J. Synthesis and characterization of nanocrystalline CoAl2O4 spinel powder by low temperature combustion. *J. Eur. Ceram. Soc.* **2003**, *23*, 2289−2295.
(40) Mohamed, R. M.; Kadi, M. W. Generation of hydrogen gas using $CuCr_2O_4$-g-C_3N_4 nanocomposites under illumination by visible light. *ACS Omega* **2021**, *6*, 4485.
(41) Alhaddad, M.; Navarro, R. M.; Hussein, M. A.; Mohamed, R. M. Bi_2O_3/g-C_3N_4 nanocomposites as proficient photocatalysts for hydrogen generation from aqueous glycerol solutions beneath visible light. *Ceram. Int.* **2020**, *46*, 24873−24881.
(42) Kadi, M. W.; Mohamed, R. M.; Ismail, A. A.; Bahnemann, D. W. H_2 production using CuS/g-C_3N_4 nanocomposites under visible light. *Appl. Nanosci.* **2020**, *10*, 223−232.
(43) Kadi, M. W.; Mohamed, R. M. Increasing visible light water splitting efficiency through synthesis route and charge separation in measoporous g-C_3N_4 decorated with WO_3 nanoparticles. *Ceram. Int.* **2019**, *45*, 3886−3893.
(44) Kadi, M. W.; Mohamed, R. M.; Ismail, A. A.; Bahnemann, D. W. Decoration of mesoporous graphite-like C_3N_4 nanosheets by NiS nanoparticle-driven visible light for hydrogen evolution. *Appl. Nanosci.* **2018**, *8*, 1587−1596.
(45) Chen, F.; Yang, H.; Wang, X.; Yu, H. Facile synthesis and enhanced photocatalytic H_2-evolution performance of NiS_2-modified g-C_3N_4 photocatalysts. *Chin. J. Catal.* **2017**, *38*, 296−304.
(46) Shawky, A.; Alhaddad, M.; Al-Namshah, K. S.; Mohamed, R. M.; Awwad, N. S. Synthesis of Pt-decorated $CaTiO_3$ nanocrystals for efficient photoconversion of nitrobenzene to aniline under visible light. *J. Mol. Liq.* **2020**, *304*, 112704.
(47) A., Shawky; M., Alhaddad; R. M., Mohamed; N. S., Awwad; H. A., Ibrahium,. Magnetically separable and visible light-active Ag/NiCo2O4 nanorods prepared by a simple route for superior photodegradation of atrazine in water. *Prog. Nat. Sci.: Mater. Int.* (**2020**, *30*), in press, DOI: DOI: 10.1016/j.pnsc.2020.01.021.
(48) Shawky, A.; Mohamed, R. M.; Mkhalid, I. A.; Awwad, N. S.; Ibrahium, H. A. One-pot synthesis of Mn_3O_4-coupled Ag_2WO_4 nanocomposite photocatalyst for enhanced photooxidative desulfurization of thiophene under visible light irradiation Appl. *Nanosci* **2020**, *10*, 1545−1554.
(49) Shawky, A.; El-Sheikh, S. M.; Rashed, M. N.; Abdo, S. M.; El-Dosoqy, T. I. Exfoliated kaolinite nanolayers as an alternative photocatalyst with superb activity. *Int. J. Chem. Environ. Eng.* **2019**, *7*, 1031745.
(50) Alhadadad, M.; Ahmed, S. Pt-decorated ZnMn2O4 nanorods for effective photocatalytic reduction of CO2 into methanol under visible light. *Cermic Int.* **2021**, *47*, 9763.
(51) Peng, S.; Ding, M.; Yi, T.; Zhan, Z.; Li, Y. Photocatalytic hydrogen evolution and decomposition of glycerol over C d0. 5 Z n0. 5 S solid solution under visible light irradiation. *Environ. Prog. Sustain. Energy* **2016**, *35*, 141−148.

https://doi.org/10.1021/acsomega.1c00872
ACS Omega 2021, 6, 10428−10436